Temperature effect on radiation-induced dislocation loops in a FCC high purity CrFeMnNi multi-principal element alloy

J.J. Gao, B. Décamps, A. Fraczkiewicz, A.C. Bach, T. Jourdan, E. Meslin

Temperature effect on radiation-induced dislocation loops in a FCC high purity CrFeMnNi multi-principal element alloy

J.J. Gao[a,*], B. Décamps[b], A. Fraczkiewicz[c], A.C. Bach[c], T. Jourdan[a], E. Meslin[a,*]

[a] Université Paris-Saclay, CEA, Service de Recherches de Métallurgie Physique, 91191, Gif-sur-Yvette, France

[b] Laboratoire de Physique des 2 infinis Irène Joliot-Curie (IJCLab), CNRS/IN2P3, (UMR9012), Université Paris-Saclay, 91405 Orsay, France

[c] MINES St-Etienne, CNRS (UMR 5307), Laboratoire Georges Friedel, LGF, 42100 Saint-Etienne, France

[*]Corresponding authors: Jingjun.gao@foxmail.com; Estelle.meslin@cea.fr

Abstract:

Temperature effect on dislocation loop density and radiation-induced segregation (RIS) phenomena are investigated on an ion irradiated 15Cr-46Fe-17Mn-22Ni (at.%) multi-principal element alloy (MPEA) over a wide range of temperatures. From 95K to 623K, loop densities are temperature independent and close to ~5.0×1022 m-3. Above 623K, loop densities decrease until ~1.05×1021 m-3 at 823K. This tendency is the same as in the conventional ternary Fe-Cr-Ni alloys. Besides, Ni enrichment and Cr, Fe, Mn depletion on loops are observed at 823K by scanning transmission electron microscopy coupled to energy dispersive X-ray spectroscopy and atom probe tomography with comparable RIS amplitude. This solute redistribution is explained by an inverse Kirkendall (IK) mechanism. In contrast, no obvious chemical segregation/depletion phenomena are detected at 298K, which reveals the temperature dependence of the IK effect. This comprehensive study of loop behavior as a function of temperature gives a better understanding of CrFeMnNi MPEAs under irradiation.

Keywords: Multi-principal element alloy; Crystal defects; Radiation-induced segregation; Ion irradiation; Dislocation loop;

Advanced irradiation-resistant materials, involving next-generation fission and future fusion reactors, need to retain high mechanical performance under extreme environments, such as high-dose radiation and/or elevated temperature [1-3]. These harsh operating environments will potentially induce structural damage in alloys and result in degradation issues, for example void swelling, radiation hardening and irradiation creep [1]. For safety margin considerations and more efficient nuclear energy systems, a novel generation of structural materials with superior radiation damage resistance is mandatory to replace some internals parts or components of the primary circuit composed by face-centered cubic (FCC) austenitic stainless steels.

A new class of metallic materials with several principal elements named high-entropy alloys (HEAs) have been drawing considerable attention due to their superior properties, such as high strength, ductility, wear resistance, and corrosion resistance [4-5]. The classical equiatomic CrFeCoNiMn HEA, named as Cantor's alloy [6], with FCC structure, was shown to exhibit good irradiation resistance [7]. However, the presence of Co leads to a high level production of the ^{60}Co radioisotope under neutron irradiation, which makes it inappropriate for a use in nuclear reactors. Therefore, some CrFeMnNi multi-principal element alloys (MPEAs) were designed, fabricated and characterized, such as 18Cr-27Fe-27Mn-28Ni, 15Cr-35Fe-15Mn-35Ni, 20Cr-40Fe-20Mn-20Ni, 18Cr-29Fe-23Mn-30Ni (all the compositions in this study are given in at.%) [8-14]. Kumar *et al.* [8] reported that in the 18Cr-27Fe-27Mn-28Ni alloy irradiated with 5.8 MeV Ni ions up to 10 dpa, loop densities monotonically decrease at elevated temperatures (from 673K to 973K, the blue solid circles in Fig.3) and the maximum mean loop size of 5.45 nm is obtained at 973K. In addition, they also hypothesized that the loop density is independent of dose and temperature between 298K to 673K with values of ~10^{23} m^{-3}. More recently, much larger loops, 27 nm for 18Cr-27Fe-27Mn-28Ni and 10 nm for 15Cr-35Fe-15Mn-35Ni irradiated by 1 MeV Kr ions up to 2 dpa at 773K, were detected by Parkin *et al.* [9], and the loop density at 50K (~4.5×10^{21} m^{-3})

was surprisingly lower than at 773K (~1.2×10^{22} m^{-3}) in irradiated 15Cr-35Fe-15Mn-35Ni samples (the green solid circles in Fig.3). What is also worth to notice that the loop densities in both 18Cr-27Fe-27Mn-28Ni (~6.7×10^{21} m^{-3}) and 15Cr-35Fe-15Mn-35Ni (~1.0×10^{22} m^{-3}) irradiated up to 0.3 dpa at 50K are nearly 10 times lower than in Kumar's study (1.5×10^{23} m^{-3}) at 298K at the same dose. Another aspect of interest is the solute redistribution in these alloys. A huge quantity of freely migrating point defects (PDs), self-interstitial atoms and vacancies, are created under irradiation. They migrate into the microstructure and may eliminate on PD sinks, giving rise to PD fluxes. Furthermore, these PDs may be coupled with solutes and, if the coupling is positive, drag solute atoms towards PD sinks [15]. This flux coupling will produce some radiation-induced segregation (RIS) phenomena at dislocation loops [14,16-17]. Up to date, only two studies reported RIS behavior near loops in CrFeMnNi MPEAs but with different results. Kamboj *et al*. [14], studied RIS phenomena in 18Cr-29Fe-23Mn-30Ni and found a significant Ni enrichment and Cr, Fe, Mn depletion on dislocation loops after irradiation with 6 MeV Fe ions up to 2 dpa at 773K using atom probe tomography (APT). However, RIS behavior on loops was not detected in neither 18Cr-27Fe-27Mn-28Ni nor 15Cr-35Fe-15Mn-35Ni irradiated with 3.7 MeV Ni ions to 75 dpa at 773K [18], with the same technique as Kamboj.

It thus appears that loop density evolution as a function of temperature and RIS behavior around loops are still under debate for CrFeMnNi MPEAs. In this work, 15Cr-46Fe-17Mn-22Ni [19] was chosen as a model alloy and irradiated in-situ within the JANNuS-Orsay platform [20] up to 0.2 dpa with a dose rate of 1.6×10^{-4} dpa/s. This low dose avoids the formation of radiation-induced damage microstructures other than dislocation loops [14], over a wide range of temperatures. The temperature effect from 95K to 823K on loop density evolution is studied comprehensively, and its effect on RIS behavior near loops is also discussed.

The high-purity 15Cr-46Fe-17Mn-22Ni (at.%) MPEA was elaborated by cold crucible induction melting at MINES Saint Etienne (EMSE, France) [19]. The alloy was firstly hot forged at 1273K, and then homogenized under argon flow at 1273K for

two hours, followed by air-cooling. Prior to irradiation, transmission electron microscopy (TEM) samples were electropolished with a solution composed of 30% nitride acid in methanol (vol.%) at 243K under 10 V. Thin foils were irradiated in-situ with 2 MeV Fe^{+} ions using a rastered beam at an ion flux of ~1.8×10^{11} ions·cm^{-2}·s^{-1} up to a fluence of ~2.5×10^{14} ions·cm^{-2} from 95K to 823K within the JANNuS-Orsay platform [20]. We calculated the damage rate by using the Iradina code [21] in Kinchin-Pease mode with a displacement energy of 40 eV. The depth profile of damage and Fe^{+} implantation profile are plotted in Fig.S1(a), the details are given in Table 1. After irradiation, the radiation-induced dislocation loops were analyzed within a 200 kV FEI TECNAI G^2 TEM. Loop densities were calculated as the surface densities of loops divided by the local thickness of the analyzed zone. The latter was estimated by the Convergent Electron Beam Diffraction (CBED) technique with **g**=<202> reflection [22-23]. Surface densities were calculated using the statistical method (details can be found in [24]). Focused Ion Beam (FIB, FEI Helio 650 NanoLab dual beam scanning electron microscope (SEM)) was applied to prepare transverse TEM thin foils, which was followed by a flash polishing technique [25] and shape atom probe tomography (APT) needles from irradiated thin foil, as shown in the schematic Fig.S1(b). Then, compositional evolutions between dislocation loops and irradiated matrix were followed by means of scanning transmission electron microscopy coupled to energy dispersive X-ray spectroscopy (STEM-EDS) in the 200 kV JEM-ARM200F TEM and APT technique. The APT needles were analyzed using a laser assisted APT (CAMECA LEAP 4000X HR) with a pulse repetition rate of 200 kHz at 50K. Laser energy pulses were set to an equivalent evaporation fraction of 20%. Reconstructions of the volumes were performed with IVAS 3.6.8 (CAMECA software) using spatial distribution maps (SDM) on low index crystallographic poles.

Before irradiation, the microstructure and composition of the as-received samples are checked with SEM-EDS (ZEISS 1525 equipped with a FEG source), as shown in Fig.S2, and the measured chemical composition is shown in Table 2. After irradiation, loop densities in the thin foils are analyzed from 95K to 823K. The damage evolution

at 823K as a function of the dose in given in supplementary. The speed rate is accelerated 100 times. We report in Fig.1 a panel of the typical kinetic bright field (KBF) loops microstructure obtained at all the investigated temperatures at the end of irradiation. At temperatures lower than 623K, the microstructure is composed of a huge density of small-sized loops (<10 nm), which appear as black dots. With increasing temperature from 623K (Fig.1(c), loop size: 28±12 nm) to 823K (Fig.1(e), loop size: 58±16 nm), the loops grow up, while their densities decrease significantly. Both faulted Frank loops and perfect loops are observed at 823K. Due to the high density and small size of loops, a statistical analysis method [24] is used to get the total number density of loops for each irradiation temperature and account for the extinction condition. This method is illustrated in Fig.2 for a sample irradiated at 823K to the final dose. Firstly, the KBF TEM micrographs are taken on the same zone with five different **g** vectors (at least two of them non-coplanar [24]), as shown in Fig.2(a)-(e). The visible loop density is calculated for each micrograph (see Fig.2f). Secondly, a system of coupled equations based on the invisibility criterion [26] is established for Frank and perfect loop families. The coupled equations are written as:

$$\begin{cases} N^{v}_{\boldsymbol{g}=\bar{1}\bar{1}1} = \frac{4}{4} N_{\boldsymbol{b}=\frac{1}{3}<111>} + \frac{3}{6} N_{\boldsymbol{b}=\frac{1}{2}<110>} \\ N^{v}_{\boldsymbol{g}=\bar{2}02} = \frac{2}{4} N_{\boldsymbol{b}=\frac{1}{3}<111>} + \frac{5}{6} N_{\boldsymbol{b}=\frac{1}{2}<110>} \\ N^{v}_{\boldsymbol{g}=0\bar{2}0} = \frac{4}{4} N_{\boldsymbol{b}=\frac{1}{3}<111>} + \frac{4}{6} N_{\boldsymbol{b}=\frac{1}{2}<110>} \\ N^{v}_{\boldsymbol{g}=022} = \frac{2}{4} N_{\boldsymbol{b}=\frac{1}{3}<111>} + \frac{5}{6} N_{\boldsymbol{b}=\frac{1}{2}<110>} \\ N^{v}_{\boldsymbol{g}=\bar{1}11} = \frac{4}{4} N_{\boldsymbol{b}=\frac{1}{3}<111>} + \frac{3}{6} N_{\boldsymbol{b}=\frac{1}{2}<110>} \end{cases}$$

in which $N^{\mathrm{v}}_{\mathbf{g}}$ is the visible loop density for the applied **g** vector, $N_{\mathbf{b}=\frac{1}{3}<111>}$ is the total density of Frank loop, and $N_{\mathbf{b}=\frac{1}{2}<110>}$ is the total density of perfect loop. Using the numerical values of loop densities, this system also can be expressed as (loops densities are in m^{-3}):

$$\begin{pmatrix} 6.12 \\ 8.19 \\ 7.60 \\ 8.21 \\ 6.15 \end{pmatrix} \times 10^{20} = \begin{pmatrix} 1 & 1/2 \\ 1/2 & 5/6 \\ 1 & 2/3 \\ 1/2 & 5/6 \\ 1 & 1/2 \end{pmatrix} \begin{pmatrix} N_{\boldsymbol{b}=\frac{1}{3}<111>} \\ N_{\boldsymbol{b}=\frac{1}{2}<110>} \end{pmatrix}$$

The least-squares method is employed to solve the system, and the error is given by standard deviation. The densities of Frank and perfect loops are respectively $N_{\mathbf{b}=\frac{1}{3}<111>}$=1.7±0.1×$10^{20}$ m^{-3} and $N_{\mathbf{b}=\frac{1}{2}<110>}$=8.8±0.1×$10^{20}$ m^{-3}. Finally, the total loop density is $N_{\text{total}}=N_{\mathbf{b}=\frac{1}{3}<111>}+N_{\mathbf{b}=\frac{1}{2}<110>}$=10.5±0.1×$10^{20}$ m^{-3}. This method is then applied to the whole batch of irradiated samples (Fig.S3 to Fig.S6). The loop density distribution as a function of temperature is plotted in Fig.3. We also gather on the same graph the loop densities from literature about conventional austenitic steels irradiated to low dose until stationary state between 298K and 873K [27-33], as well as reported CrFeMnNi MPEAs [8-9]. This graph demonstrates the similar evolution of loop density between the studied MPEA in this work and the conventional stainless steels. From 95K to 623K, the loop density is nearly constant (~5.0×10^{22} m^{-3}) and is temperature independent. Above 623K, it decreases drastically to reach 1.1±0.2×10^{22} m^{-3} at 723K and 10.5±0.1×10^{20} m^{-3} at 823K. It is worth noticing that the loop density at 95K (1.7±0.2×10^{22} m^{-3}) is a bit lower than at 298K (5.0±0.1×10^{22} m^{-3}), this could come from a poor contrast of small defects and/or overlapping effects arising from a rather thick working area (~220 nm) at 95K [8,34].

In order to study RIS phenomena near dislocation loops, STEM-EDS is firstly applied on the 823K sample with investigated loops edge-on. As a consequence, the FIB lamella is oriented on the [001] zone axis, in which only one third of the perfect <110> type loop planes are parallel to the incident electron beam. The STEM-BF image and corresponding EDS Ni mapping (Fig.S7) show that Ni enrichment occurs at each visible dislocation loop, and the strongest enrichment corresponds to edge-on loops. RIS amplitude has then been quantitatively estimated on one edge-on perfect loop. Fig.4(a) is a STEM-BF image taken from the FIB lamella on z=[001] zone axis, Fig.4(b)

exhibits a perfect loop (loop circled in green circle in Fig.4(a)) in the edge-on orientation. The composition profiles across the loop habit plane along the arrow (in Fig.4(b)) are shown in Fig.4(c), and chemical segregation behavior with substantial Ni enrichment and Cr, Fe, Mn depletion is observed. The corresponding STEM-EDS mappings are shown in Fig.S8. To confirm this STEM-EDS measurement and get a better spatial distribution of atoms along loop plane, APT analyses have been performed. Dislocation loops are investigated indirectly through their possible chemical redistribution in the vicinity of loops. They are decorated by enriched/depleted elements and, as a result, can be easily identified. Fig.5(a) illustrates a 3D reconstructed APT volume extracted 230 nm away from the surface after irradiation at 298K. No obvious segregation/depletion is detected in the investigated volume. The composition profiles in Fig.5(b) also show that the chemical composition of the sample is identical to the composition of the as-received one measured by SEM-EDS (solid line is mean value, dashed line is the error bar). However, disk-shaped segregations at 823K are obtained in Fig.5(c) and are comparable to those detected in Fig.4(c), providing further confidence that the object intercepted by APT is a dislocation loop. In order to highlight chemical evolution between the adjacent matrix and the loop, a cylinder is inserted perpendicular to this investigated loop (Fig.S9) and the concentration profiles confirm the segregation in Ni and depletion in Cr, Fe and Mn around the loop (Fig.5(d)). Our STEM-EDS and APT results reveal a good agreement on chemical segregation/depletion amplitude (Fig.5(d)).

In irradiated alloys, RIS phenomena is driven by a coupling with vacancies or self-interstitial atoms (SIAs). In concentrated alloys, the vacancy mechanism is usually considered and is related to the well-known inverse kirkendall (IK) effect, as in austenitic stainless steels. When RIS occurs through an IK effect, slow diffusers segregate while fast diffusers deplete at defect sinks [35]. It is linked to the preferential exchange of a solute with vacancy flux. The flux of a particular atom is proportional to the local atomic concentration, the vacancy diffusivity and the solute self-diffusion coefficient [36]. Thanks to the investigation of radiotracer thermal diffusivity

coefficients for all the elements in equiatomic CoCrFeNiMn HEA at elevated temperatures [37], it is well known that the order of the self-diffusion coefficients is: $D_{Mn}>D_{Cr}>D_{Fe}>D_{Ni}$. Thus, we expect the fastest diffuser Mn to deplete and the slowest one Ni to enrich on loops, as observed in our study. Depletion or enrichment of Cr and Fe are dependent on the Cr self-diffusion coefficient (D_{Cr}) and Fe self-diffusion coefficient (D_{Fe}) relative to the average self-diffusion coefficient (D_a) in the alloy: if $D_{(Cr/Fe)}/D_a>1$, Cr/Fe will deplete, otherwise Cr/Fe will enrich. In the present study, Cr and Fe deplete in our study. This is consistent with the result obtained in the irradiated FeNiMnCrCo HEA, in which slower diffusers (Ni, Co) enriched while faster diffusers (Cr, Fe, Mn) depleted at sinks [16-17]. It is also worth to mention that the shape of the Fe profiles obtained in Fig.4(c) and Fig.5(d) are not the typical "V-shape", which is usually obtained from solute depletion driven by IK mechanism, but a "W-shape" [8,38], a transient state before the stationary state "V-shape" [39]. Finally, as already mentioned, there are no obvious segregation phenomena detected by APT at 298K. At this low temperature, vacancy diffusivity at 298K is probably not large enough to permit any significant IK effect on dislocation loops. Therefore, no RIS phenomena are detected at clusters in the 298K sample.

In summary, temperature effect on loop density evolution in 15Cr-46Fe-17Mn-22Ni has been carefully investigated between 95K and 823K for the first time: loop densities are temperature independent and are close to ~5.0×10^{22} m^{-3} from 95K to 623K. Above 623K, loop densities decrease monotonically down to ~1.05×10^{21} m^{-3} at 823K. It shows the same trend within conventional ternary Fe-Cr-Ni alloys. Besides, RIS near loops indicates a temperature dependent behavior: Ni enrichment and Cr, Fe, Mn depletion are observed probably driven by IK mechanism at 823K by STEM-EDS and APT with comparable RIS amplitude. In contrast, no obvious chemical segregation/depletion phenomena are detected at 298K, where IK effect is probably not activated. This comprehensive study of loop behavior as a function of temperature gives a better understanding of CrFeMnNi MPEAs under irradiation.

Acknowledgments

This research is funded by the ANR-PRCE-HERIA project (ANR-19-CE08-0012-01). Claude Varillon and Mickaël Haering (MINES St-Etienne) are acknowledged for the alloys elaboration. We acknowledge the JANNuS-Orsay platform (IJCLab, Paris-Sac/CNRS, Orsay, France) for offering *in-situ* ion radiation facility. In particular, S. Jublot-Leclerc and C. Baumier are acknowledged for their help and advice during the experiments. Irradiation was also supported by the EMIR&A French accelerator network and by the GENESIS EQUIPEX Program [PIA, ANR (ANR-11-EQPX- 0020)] and Normandie Region.

References

[1] S.J. Zinkle, G.S. Was, Acta Materialia 61 (2013) 735–758.
[2] S.J. Zinkle, J.T. Busby, Materials Today 12 (2009) 12–19.
[3] S.J. Zinkle, L.L. Snead, Annual Review of Materials Research 44 (2014) 241–267.
[4] F. Otto, A. Dlouhý, Ch. Somsen, H. Bei, G. Eggeler, E.P. George, Acta Materialia 61 (2013) 5743–5755.
[5] E.P. George, D. Raabe, R.O. Ritchie, Nat Rev Mater 4 (2019) 515–534.
[6] B. Cantor, Entropy 16 (2014) 4749–4768.
[7] Z. Zhang, D.E.J. Armstrong, P.S. Grant, Progress in Materials Science 123 (2022) 100807.
[8] N.A.P.K. Kumar, C. Li, K.J. Leonard, H. Bei, S.J. Zinkle, Acta Materialia 113 (2016) 230–244.
[9] C. Parkin, M. Moorehead, M. Elbakhshwan, J. Hu, W.-Y. Chen, M. Li, L. He, K. Sridharan, A. Couet, Acta Materialia 198 (2020) 85–99.
[10] B.B. Bian, N. Guo, H.J. Yang, R.P. Guo, L. Yang, Y.C. Wu, J.W. Qiao, Journal of Alloys and Compounds 827 (2020) 153981.
[11] M.A. Tunes, G. Greaves, H. Bei, P.D. Edmondson, Y. Zhang, S.E. Donnelly, C.G. Schön, Intermetallics 132 (2021) 107130.
[12] A. Fernández-Caballero, E. Bousser, S.M. Shubeita, P.T. Wady, Y. Gu, R. Krishna, M.J. Gorley, D. Nguyen-Manh, P.M. Mummery, E.J. Pickering, Nuclear Materials and Energy 28 (2021) 101028.
[13] M.A. Tunes, H. Le, G. Greaves, C.G. Schön, H. Bei, Y. Zhang, P.D. Edmondson, S.E. Donnelly, Intermetallics 110 (2019) 106461.
[14] A. Kamboj, E.A. Marquis, Scripta Materialia 215 (2022) 114697.
[15] L. Messina, T. Schuler, M. Nastar, M.-C. Marinica, P. Olsson, Acta Materialia 191 (2020) 166–185.

[16] M.-R. He, S. Wang, S. Shi, K. Jin, H. Bei, K. Yasuda, S. Matsumura, K. Higashida, I.M. Robertson, Acta Materialia 126 (2017) 182–193.
[17] W.-Y. Chen, J.D. Poplawsky, Y. Chen, W. Guo, J.-W. Yeh, Materialia 14 (2020) 100951.
[18] C. Parkin, M. Moorehead, M. Elbakhshwan, X. Zhang, P. Xiu, L. He, M. Bachhav, K. Sridharan, A. Couet, Journal of Nuclear Materials 565 (2022) 153733.
[19] M. Traversier, P. Mestre-Rinn, N. Peillon, E. Rigal, X. Boulnat, F. Tancret, J. Dhers, A. Fraczkiewicz, Materials Science and Engineering: A 804 (2021) 140725.
[20] C.-O. Bacri, C. Bachelet, C. Baumier, J. Bourçois, L. Delbecq, D. Ledu, N. Pauwels, S. Picard, S. Renouf, C. Tanguy, Nuclear Instruments and Methods in Physics Research Section B: Beam Interactions with Materials and Atoms 406 (2017) 48–52.
[21] J.-P. Crocombette, C.V. Wambeke, EPJ Nuclear Sci. Technol. 5 (2019) 7.
[22] K. Ma, B. Décamps, A. Fraczkiewicz, T. Jourdan, F. Prima, M. Loyer-Prost, Acta Materialia 212 (2021) 116874.
[23] B.A. CARTER, D.B. Williams, C.B. Carter, D.B. Williams, Transmission Electron Microscopy: A Textbook for Materials Science. Diffraction. II, Springer Science & Business Media, 1996.
[24] A. Prokhodtseva, B. Décamps, A. Ramar, R. Schäublin, Acta Materialia 61 (2013) 6958–6971.
[25] B. Horváth, R. Schäublin, Y. Dai, Nuclear Instruments and Methods in Physics Research Section B: Beam Interactions with Materials and Atoms 449 (2019) 29–34.
[26] J.F. Ziegler, Nuclear Instruments and Methods in Physics Research Section B: Beam Interactions with Materials and Atoms 219–220 (2004) 1027–1036.
[27] T. Okita, T. Sato, N. Sekimura, T. Iwai, F.A. Garner, Journal of Nuclear Materials 367–370 (2007) 930–934.
[28] A. Etienne, M. Hernández-Mayoral, C. Genevois, B. Radiguet, P. Pareige, Journal of Nuclear Materials 400 (2010) 56–63.
[29] Q. Xu, H. Watanabe, N. Yoshida, Journal of Nuclear Materials 233–237 (1996) 1057–1061.
[30] H.F. Huang, J.J. Li, D.H. Li, R.D. Liu, G.H. Lei, Q. Huang, L. Yan, Journal of Nuclear Materials 454 (2014) 168–172.
[31] T.M. Williams, Journal of Nuclear Materials 88 (1980) 217–225.
[32] T.M. Williams, Journal of Nuclear Materials 79 (1979) 28–42.
[33] D.J. Edwards, E.P. Simonen, S.M. Bruemmer, Journal of Nuclear Materials 317 (2003) 13–31.
[34] S.J. Zinkle, Y. Matsukawa, Journal of Nuclear Materials 329–333 (2004) 88–96.
[35] M. Nastar, F. Soisson, in: Comprehensive Nuclear Materials, 2012, pp. 471–496.
[36] T.R. Allen, J.T. Busby, G.S. Was, E.A. Kenik, Journal of Nuclear Materials 255 (1998) 44–58.

[37] M. Vaidya, K.G. Pradeep, B.S. Murty, G. Wilde, S.V. Divinski, Acta Materialia 146 (2018) 211–224.
[38] S.M. Bruemmer, E.P. Simonen, P.M. Scott, P.L. Andresen, G.S. Was, J.L. Nelson, Journal of Nuclear Materials 274 (1999) 299–314.
[39] M. Nastar *, Philosophical Magazine 85 (2005) 641–647.

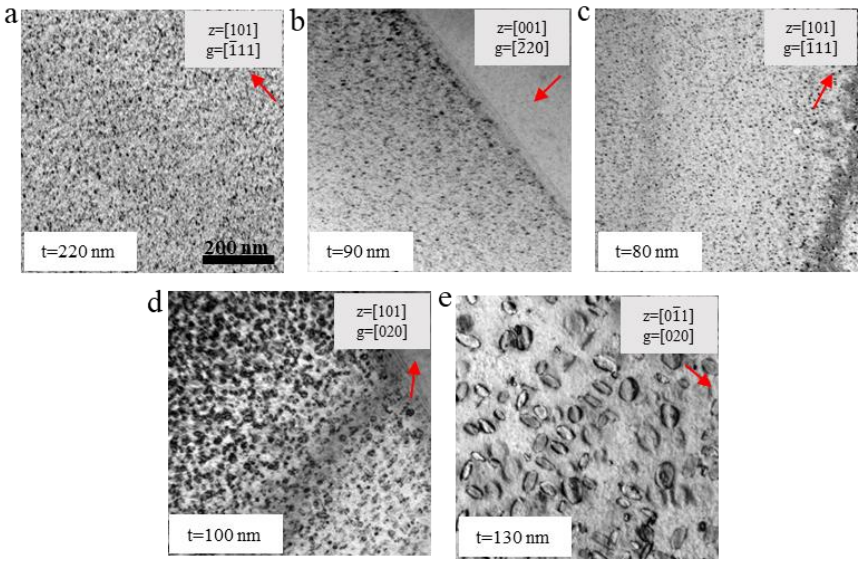

Fig.1 Kinetic BF TEM micrographs of irradiation-induced defects to the final dose at (a) 95K, (b) 298K, (c) 623K, (d) 723K, (e) 823K. "t" is the thickness of the zone observed.

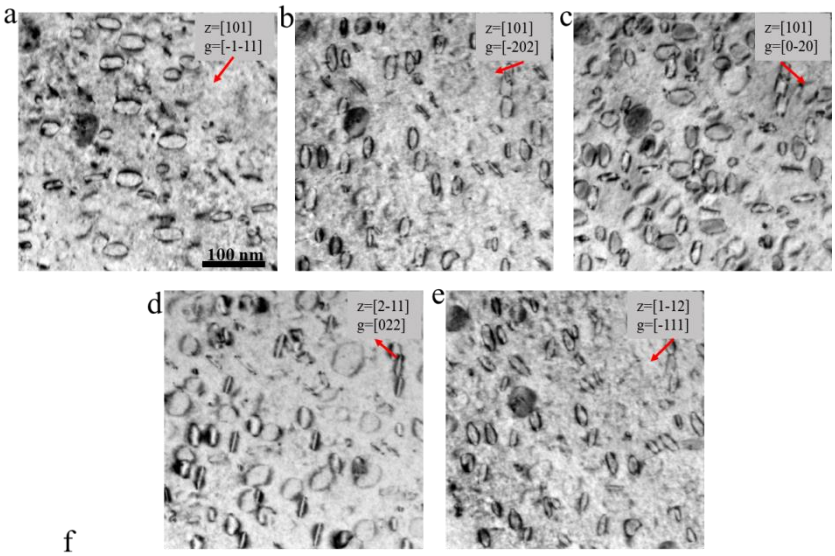

Zone axis	[101]			[2-11]	[1-12]
g	-1-11	-202	0-20	022	-111
Loop density ($10^{20}m^{-3}$)	6.12±0.94	8.19±1.11	7.60±1.06	8.21±1.10	6.15±0.93

Fig.2 Dislocation loop density calculation by statistic method [24] of the sample irradiated to the final dose at 823K: (a-e) KBF TEM micrographs of the same zone showing visibility of loops under five **g** vectors; (f) calculated loop density with five different **g** used for statistic analysis.

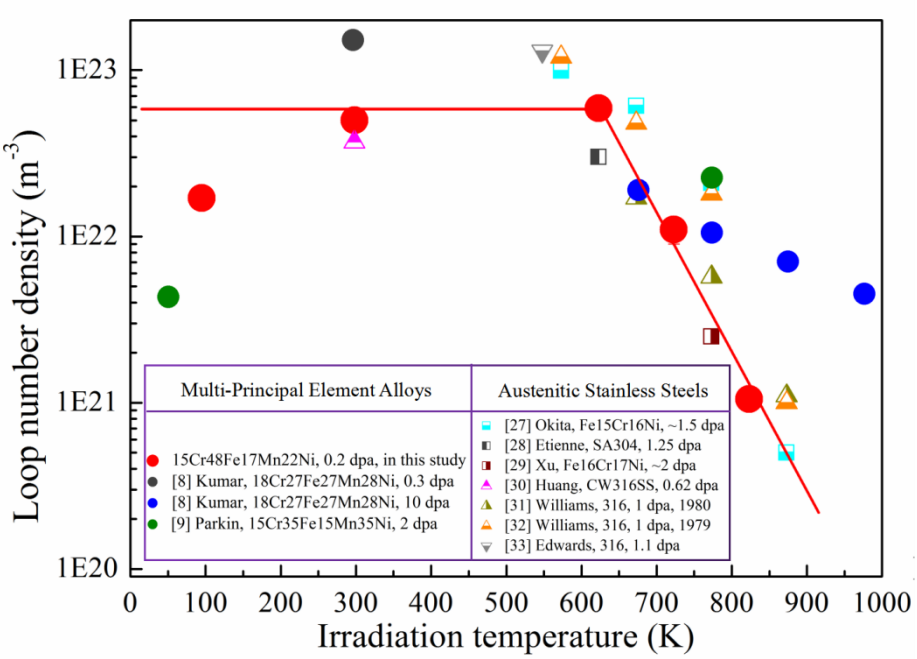

Fig.3 Evolution of dislocation loop density as a function of ion irradiation temperature.

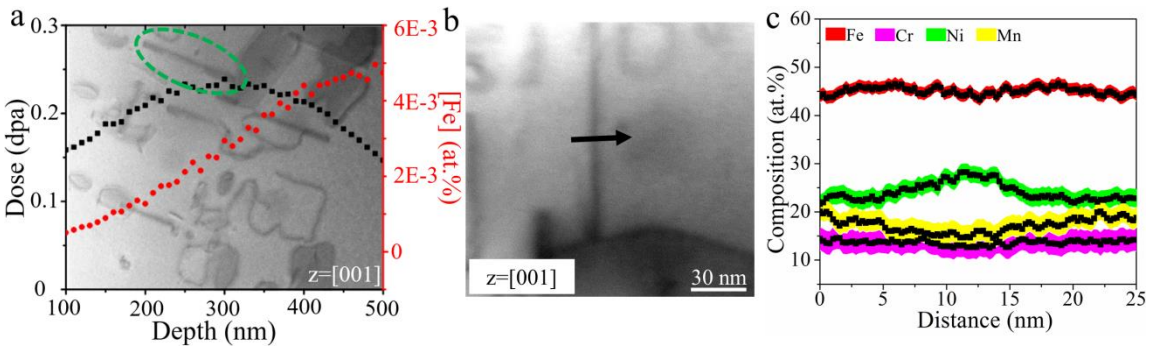

Fig.4 RIS on a dislocation loop at 823K by STEM: (a) STEM-BF image of FIB lamella on z=[001] zone axis superimposed with damage (in black) and implanted (in red) ion depth profiles; (b) STEM-BF micrograph of the zoomed edge-on loop in (a); (c) composition profiles across the loop along arrow in (b).

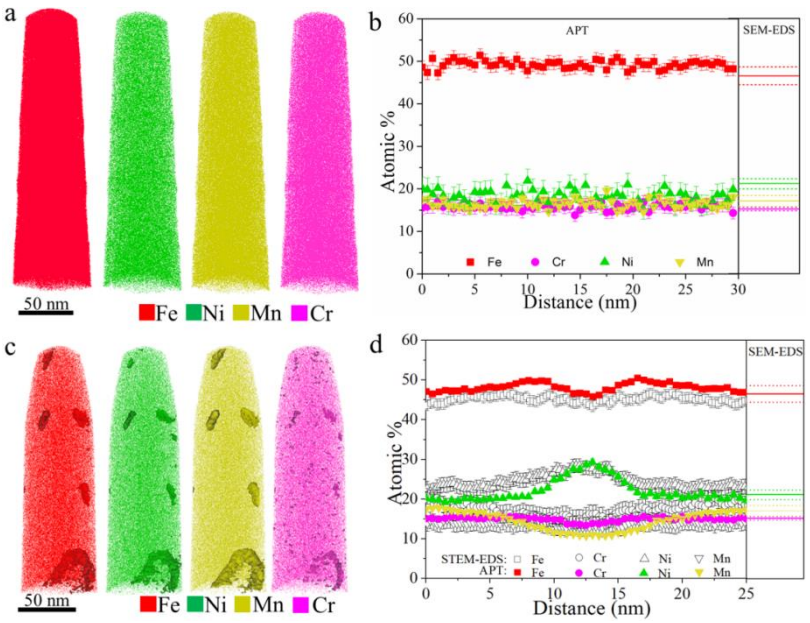

Fig.5 APT results of irradiated specimen: (a) APT reconstructed volume (80×80×230 nm^3) and (b) corresponding concentration profiles at 298K; (c) 3D distribution of Fe, Ni, Mn, Cr (60×60×200 nm^3) and (d) concentration profiles between matrix and dislocation loop at 823K.

Tables:

Table 1: Summary of ion irradiation conditions for the 15Cr-46Fe-17Mn-22Ni MPEA.

Ion	Dose (dpa) (at peak)	Dose rate (dpa/s) (at peak)	Temperature (K)
Fe^{+} 2 MeV	0.2	$1.6\ 10^{-4}$	95, 298, 623, 723, 823

Table 2: Chemical composition of the 15Cr-46Fe-17Mn-22Ni alloy, as-received from EMSE (nominal composition). Measurements have been performed by SEM/EDS.

at.%	Fe	Ni	Cr	Mn
15Cr-46Fe-17Mn-22Ni	46.5±2.1	21.1±1.2	15.2±0.4	17.3±1.3